1 # Supplementary Information

2 ## S1 Time domain thermoreflectance (TDTR)

3 ### S1.1 Setup, thermal modelling fits and sensitivity analysis

4 The setup utilized to probe thermal conductivity is shown in Fig. S1.1. Sensitivity analysis shown in Fig.

5 S1.2 is performed to analyze highest sources of uncertainties accurately and quantitatively. These

6 uncertainties strongly influence TDTR signals and impact the accuracy to which thermal conductivity can

7 be precisely estimated and therefore need to be eliminated either by using known reference values or by

8 accurately fitting using fit to data as shown in Fig. S1.3. thermal conductivity denoted by κ_z (W/mK) and
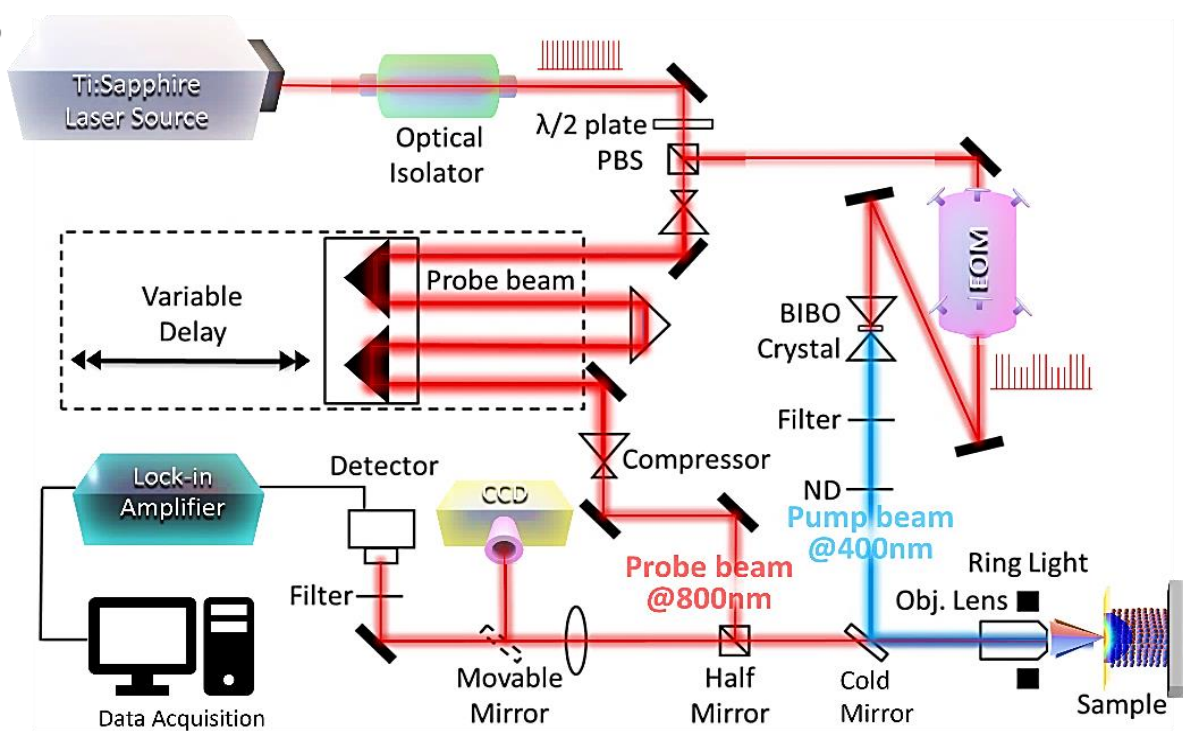

Figure S1.1: Experimental setup for thermal conductivity characterization

9 volumetric specific heat capacity denoted by Cp_{vhc} (J/m^3).

10

11 ## S1.2 Picosecond acoustics

12 We used picosecond acoustics echoes in our TDTR reflectivity data for investigating the velocity of sound

13 propagation in samples pre and post intercalation. These echoes can be used to determine the speed at which

14 sound waves propagate through them. The velocity of sound propagation (v) in a material can be calculated

15 using the formula: $v = 2d / t$, where d is the thickness of the material and t is the time it takes for the acoustic

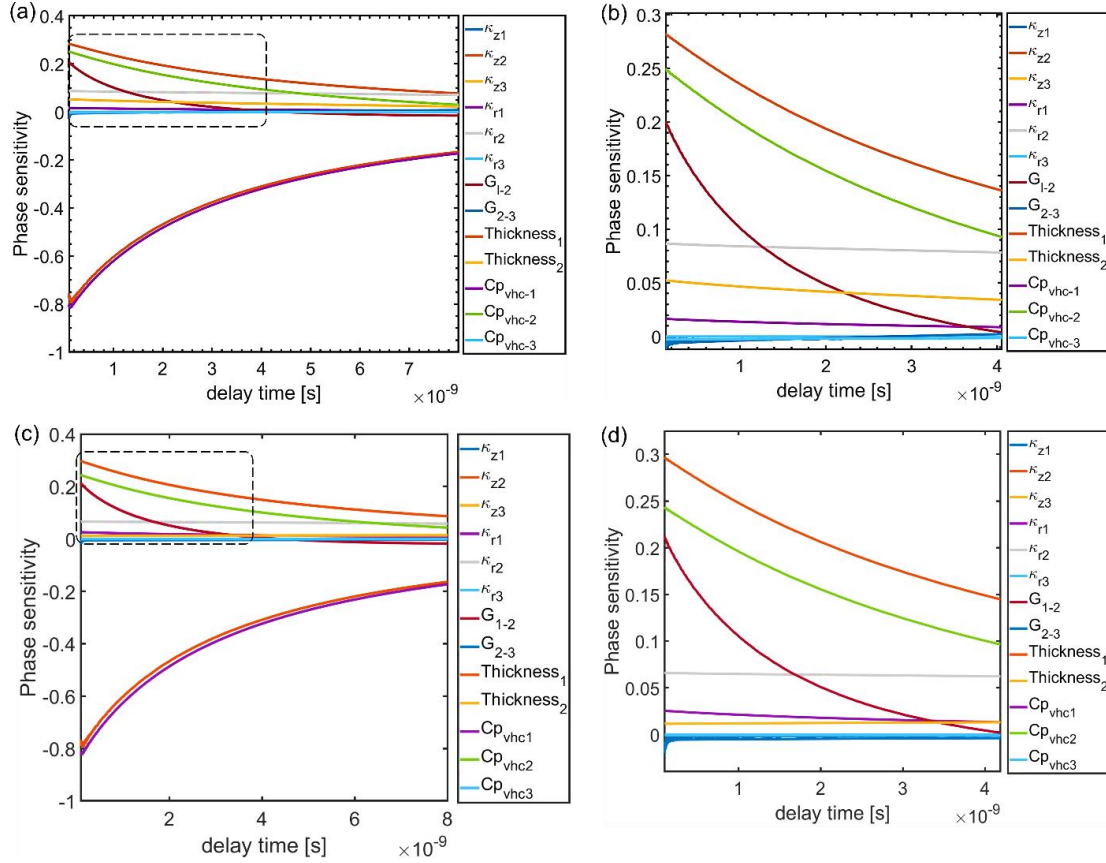16 wave to travel through the material.

Figure S1.2:. Sensitivity analysis pre and post intercalation. (a) Sensitivity calculation for 450 nm graphite film for different thermal properties involved with dashed region magnified in (b) from 0ns to 4 ns revealing 2 highest sensitive parameters namely κ_z and Cp_{vhc}. (c) Sensitivity calculation for 710 nm GIC film (intercalated counterpart of 450 nm) for different thermal properties involved with dashed region magnified in (d) from 0ns to 4 ns revealing 2 highest sensitive parameters namely κ_z and Cp_{vhc} .
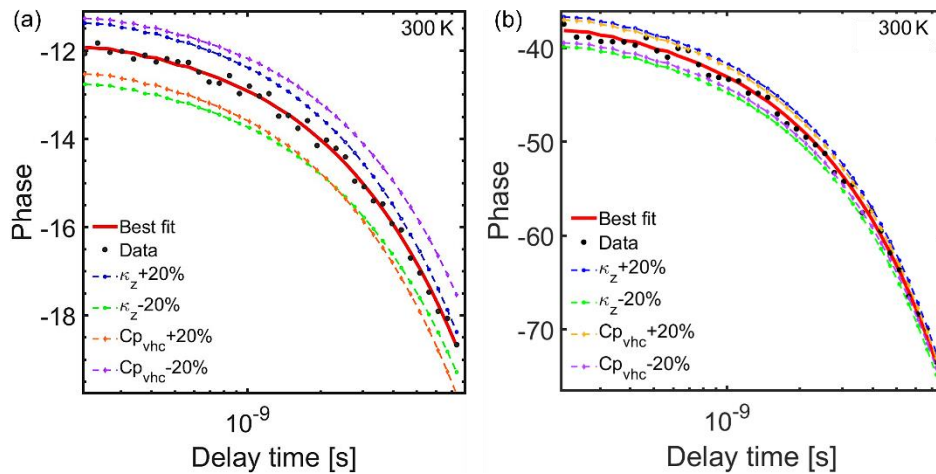

Figure S1.3: A typical thermal fit result at 300K of TDTR measurement for a 450 nm thick graphite in (a) and its intercalated counterpart of 700 nm thickness in (b). The phase data of TDTR measured signal for both cases are compared with the thermal modelling fit and presented along with the $\pm 20\%$ bounds of the best-fitted value by varying most sensitive parameters that affect TDTR signal namely κ_z and Cp_{vhc}.

S2 Quantitative detection of Mn concentration using ICP-OES method

S2.1. Sample preparation and reagents

To detect traces of Mn in $FeCl_3$ powder using inductively coupled plasma optical emission spectrometry ICP-OES Agilent 5100, the following materials and reagents were utilized: $FeCl_3$ powder, High purity deionized water and acid digestion reagent (nitric acid, HNO_3). Table S2.1 presents two of several samples we prepared and details sample preparation for subsequent calibration and measurement.

	Sample preparation steps	Higher concentration sample*(column B)* (to be used for Mn detection)	Lower concentration sample*(column C)* (to be used for Fe detection)
1	empty bottle/g	17.8144	17.8775
2	FeCl₃ powder in mg + weighing dish in mg	100.031	100.031
3	Weighing dish/mg	4.742	4.742
4	Prepared solution for Fe detection/g		0.96
5	FeCl₃ (only powder)/mg	95.289	
6	Prepared solution and bottle/g	118.5143	116.968 (C4 is diluted with 100mL water)
7	Prepared solution/g	100.6999	99.0905
8	ppm (FeCl3)	1149.646	13.962

Table S2.1: Table outlining sample preparation steps involved to detect Mn in $FeCl_3$ powder from solution prepared. Two types of samples are used: 2nd column that contains the Higher concentration sample (to be used for Mn detection)- lets refer to as column B, and the last column that represents the highly diluted much lower concentration sample (to be used for Fe detection)- lets refer to as column C. The primary purpose of the analysis is to detect traces of Mn in the $FeCl_3$ powder. Column B, which contains the Mn of interest, is not diluted to allow for better detection of trace amounts of Mn. The concentrations in column B are within the detection range of the ICP-OES instrument, so further dilution is not required. Column C is heavily diluted to serve as a reference or control sample for the Fe detection. The dilution helps to separate the signals from Mn and Fe in the ICP-OES analysis.

	Detected element	Iterations	Low Concentration sample measured @λ=238.204 nm	Low Concentration sample measured @λ=239.563 nm	Low Concentration sample measured @λ=261.187 nm	High Concentration sample measured @λ=257.610 nm	High Concentration sample measured @λ=259.372 nm	High Concentration sample measured @λ=260.56 nm
1	Fe	1st	2.5 ppm	2.482	2.472	--	--	--
2	Fe	2nd	2.841 ppm	2.838	2.829	--	--	--
3	Fe	3rd	3.172 ppm	3.126	3.131	--	--	--
4	Mn	1st	--	--	--	0.769	1.138	0.742
5	Mn	2nd	--	--	--	0.836	1.236	0.814
6	Mn	3rd	--	--	--	0.943	1.399	0.914

Table S2.2: Concentration results obtained after the ICP-OES measurement for detecting Mn (manganese) in $FeCl_3$ (ferric chloride) powder. The table presents the concentration (in parts per million, ppm) of Fe and Mn at different wavelengths. Optimal wavelength for detecting Fe comes out to be 238.204 nm and that for Mn is 257.610 nm. Dark bordered cells corresponding to samples for Fe and Mn present their measured concentrations in ppm.

In the above table, the important data are the 1st-3rd iterations values in the @238.204 nm column and the 1st-3rd iterations values in the @257.61 nm column. The reason for this is that these specific wavelengths correspond to the most sensitive and accurate detection of Fe and Mn in the ICP-OES measurement.

These values represent the concentrations of Mn in the prepared high concentration samples at the 257.610 nm wavelength, which is the optimal wavelength for detecting Mn in this experiment.

In summary, the table presents the ICP-OES measurement results for detecting Mn in $FeCl_3$ powder. The critical data points are the Fe and Mn concentrations at their respective optimal wavelengths (Fe 238.204 nm and Mn 257.610 nm). These values provide the most accurate information for analyzing the presence and concentrations of Fe and Mn in the samples.

From table S2.1, the solution for Fe determination is adjusted to 14 ppmw with $FeCl_3$, The Fe equivalent 4.8 ppmw. Mn is about 0.0333 (1/30) times the mass of iron (Fe). . This implies the Mn concentration is around 0.16 ppmw.

From ICP results we can deduce Fe:Mn $|_{ICP} \sim 300$, $FeCl_3$:Mn $|_{ICP} \sim 100:0.08$.

S2.2. Comparing SEM-EDX wt% result of co-GIC and ICP-OES wt% result on powder

Mn/Fe $|_{EDX\ GIC} = 0.02 \gg$ Mn/Fe $|_{ICP\ powder} = 1/300=0.003$ clearly demonstrates 1-order stark contrast, thus clearly affirming the strong preferential selectivity towards Mn with the current process window.

Based on the SEM EDX result on Table S2.3 the Mn/Fe ratio in the GIC sample being 0.02 and the ICP-OES result of the Mn/Fe ratio in the $FeCl_3$ powder being 0.002. Consequently, we see Mn preferably

more intercalated than $FeCl_3$ in interlayers of graphite as presented in EELS STEM mapping result Fig. 2 (j). This can be attributed to our finding that Mn/Fe ratio in the GIC is significantly higher than the Mn/Fe ratio in the $FeCl_3$ powder, which supports the preferential diffusion of Mn over $FeCl_3$ within the graphite layers. Therefore, the EELS STEM mapping result is consistent with the SEM EDX and ICP-OES results. The selectivity could possibly result from current experimental process window.

Element	At%	Wt%	Wt% SD
C	51.64	30.2	0.32
O	0.48	0.37	0.05
Si	41.86	57.42	0.35
Cl	4.53	7.84	0.07
Mn	0.03	0.08	0.01
Fe	1.46	3.98	0.27

Table S2.3: EDX wt% result on our CO-GIC sample

S3- Atomic-resolution electron microscopy STEM and EELS

The oxidation state of Manganese is determined to be 2+ based on the integral intensity ratio presented in Figure S3.2. Our results on measured peak position and integral intensity ratio shown in Fig S3.2(b,c) agree well with the literature results shown in Fig S3.1(a). Furthermore we deduce the elemental concentration ratio to be C : Cl : Mn : Fe = 77 : 14.6 : 7.0 : 0.97. We find our samples exhibit +2 Mn state on comparing our result with literature. This implies some possible reaction of Mn with another element and it safe to assume Mn reacts with Cl_2 to form our observed layers of $MnCl_2$ at the process parameters we employed for intercalation that seem to predominantly favour Mn to intercalate more readily than Fe.
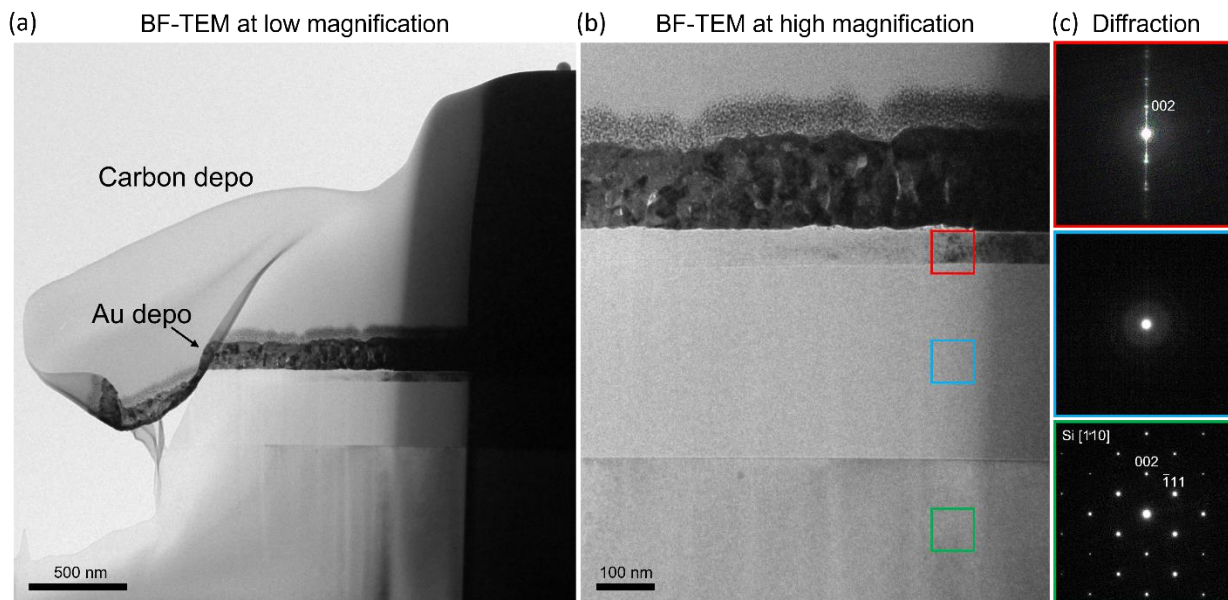
Figure S3. 1: Bright-Field TEM images and Diffraction spots at different regions of sample prepared for TEM and EELS imaging. (a-b) Bright-field TEM image at low and high magnification respectively. (c) Characteristic signature diffraction spots for graphite(red) region, substrate consisting of SiO2(blue square region) and silicon (green region) respectively corresponding to colored regions marked in (b).
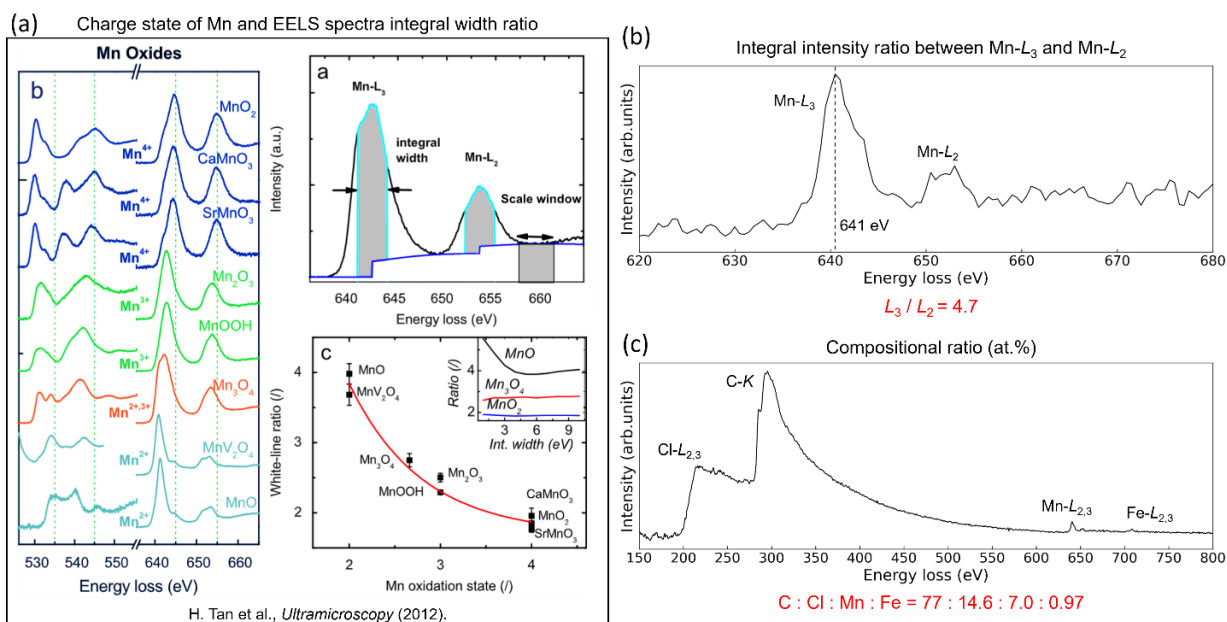
85

Figure S3. 2: Analyzing EELS spectra to investigate charge state of Mn present in our sample. (a)Various EELS profiles corresponding to multiple oxidation states Mn can possess in different compounds revealing sharply decreasing trend of integral intensity ratio with oxidation state. (b) Our result yields integral intensity ratio of 4.7 confirming +2 oxidation state (c)Elemental concentration ratio turns out to be C : Cl : Mn : Fe = 77 : 14.6 : 7.0 : 0.97.

86

S4 - Determining Stage 3 large area uniformity using Raman mapping

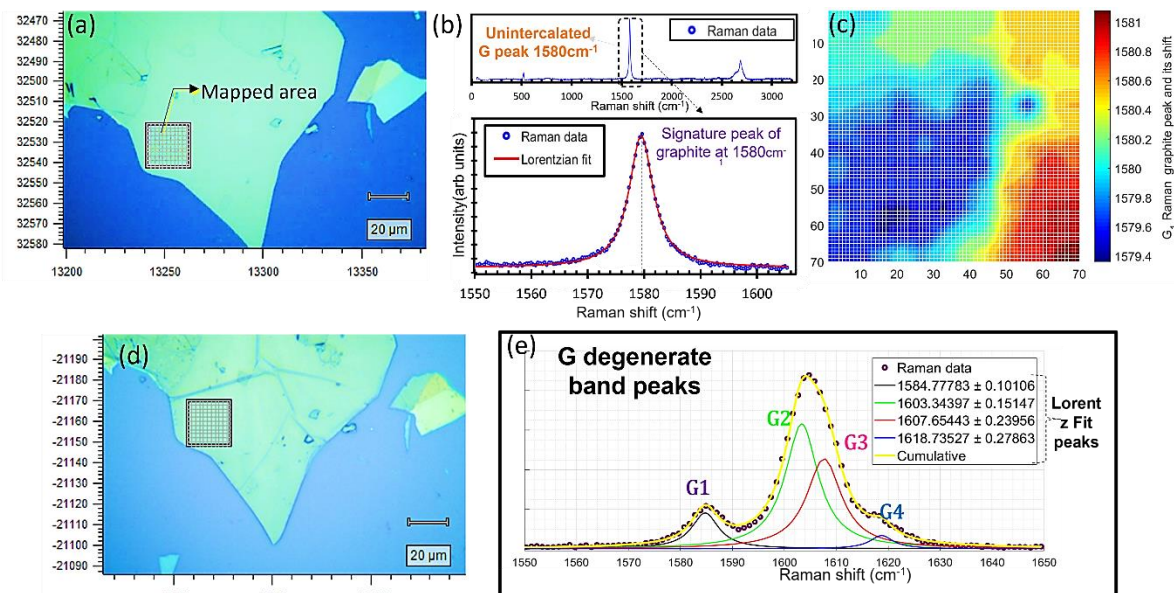88 Spatial mapping of G peak before and after intercalation is characterized using Raman Spectroscopy

Figure S4. 1: Sample regions defined for mapping(a,d) before and after intercalation and their respective Raman spatial mapping averaged out results(b,e) revealing signature peaks for graphite and dominant stage-3 GICs respectively.

89 revealing homogenous stage 3 distribution in figure S4.1. Upon averaging the spatial G peak positions, we

90 find blue-shift of G peak from 1580 cm^{-1} to 1605 cm^{-1} thus suggesting *stage-3* over a large area.

91

92

93

94

95

96

97

98

S5 - Mapping elemental chemical composition GIC and powder

Scanning electron microscopy (SEM; JEOL JSM-6610LV) and energy dispersive X-ray spectroscopy (EDS; JEOL JED-2300) was used to examine the elemental chemical compositional mapping of intercalant powder and co-GIC samples as shown in Fig S5.1 andFigure **S5.** respectively.
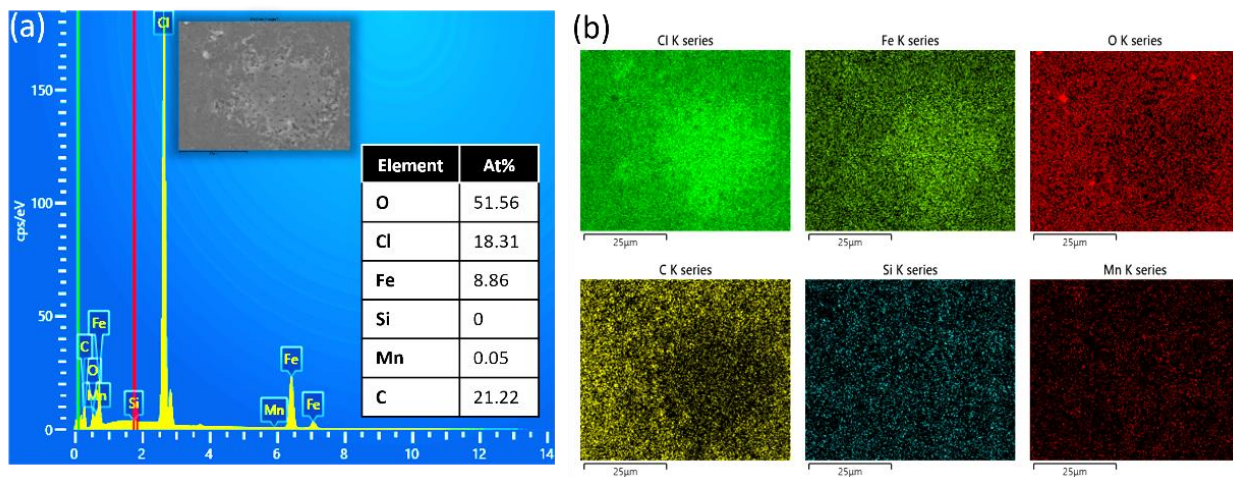

Figure S5. 1: SEM EDX scans of powder. (a)EDX spectra showing elemental peaks Also shows the electron image of area scanned. (b)EDX elemental mapping of region being probed.
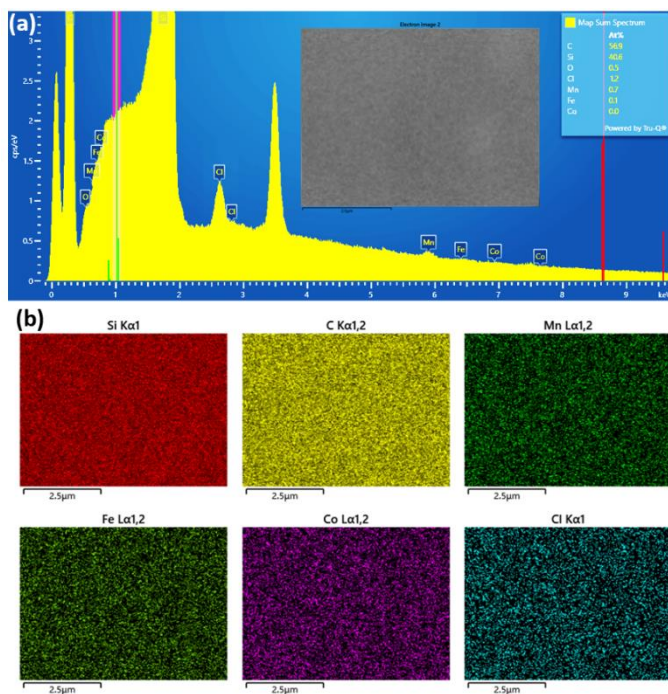

Figure S5.2: SEM EDX scans and elemental mappings of a GIC from same batch as samples investigated in the main text for thermal conductivity. EDX spectra showing all elemental peaks with atomic percentages proportion in table.

S6- Debye-Callaway modelling

S6.1: Phonon Scattering rates and modelling thermal conductivity

The Debye model of thermal conductivity considers both normal (N) and Umklapp (U) processes[1]; however, when calculating the overall scattering relaxation rate (or the associated relaxation lifetime) of phonons, the model considers only the single-mode relaxation time, which neglects the momentum-conserving characteristic of N processes. To calculate the effective scattering rate of phonons, Callaway[2] incorporated the momentum-conserving character of N processes as a crucial component of lattice thermal transport. The resulting thermal conductivity expression includes an extra term (other than the Debye term) known as the N-drift or Callaway term.

Relaxation times of three-phonon scatterings are often parametrized by expressions of the following type [33,34]:

$$\tau_{anh}^{-1} = B_T \omega^m T^n \tag{S1}$$

where $m + n = 5$ and B_T is a constant over a particular temperature range. In this study, the low-temperature form of the intrinsic phonon-phonon scattering rate was applied using a semi-empirical parameterized expression, assuming the N and U processes to exhibit the same frequency dependence, as follows [20,21]:

$$\tau_{anh}^{-1} = \left[B_N + B_U \, exp\left(-\frac{\theta_D}{\alpha T}\right)\right] \omega^2 T^3, \tag{S2}$$

where B_N and B_U are anharmonic coupling constants or anharmonic strength pre-factors for three-phonon N and U processes that yield parametrized τ_N^{-1} and τ_U^{-1} expressions, respectively, θ_D is the average Debye temperature for all acoustic branches, and α is a constant.

The scattering rate for phonon scattering due to defects that are significantly larger than the phonon wavelength (such as boundaries) is expressed as the following:

$$\tau_B^{-1} = \frac{v}{\lambda_B}, \tag{S3}$$

where the boundary scattering length is denoted by λ_B, which represents actual thickness of sample before and after intercalation was used as the scattering length and is assumed to be the same for all phonons, and τ_B^{-1} is independent of the phonon frequency ω and temperature T.

The scattering rate for phonon scattering induced solely by the reduction in the characteristic length is expressed as the following:

133 $$\tau_{intc}^{-1} = \frac{v}{\lambda_{intc}},$$ (S4)

134 where the intercalation scattering length is denoted by λ_{intc}, which represents an effective length that is

135 determined from a low-temperature fit of data to the κ_z–T trend of the samples and is assumed to be the

136 same for all phonons, and τ_{intc}^{-1} is independent of the phonon frequency ω and temperature T.

137 Subsequently, a parametric formulation based on Rayleigh scattering, a law that is followed by

138 impurities, was used to model scattering phenomena due to impurities. Therefore, the scattering rate due to

139 impurity phonon scattering were expressed by the following:

140 $$\tau_{Imp}^{-1} = A\omega^4,$$ (S5)

141 where A is the impurity-scattering strength constant or Rayleigh scattering strength, which is estimated by

142 fitting the experimental data to the full Debye-Callaway model, and is usually predominant near $T_{max.}$

143 Subsequently, the spectral Matthiessen's rule, which is commonly used to quantify the total spectral

144 scattering rate when multiple scattering mechanisms operate simultaneously in the system, was used for

145 analysis, assuming all scattering events to be independent. Thus, the total resistive relaxation rate or

146 scattering rate, τ_C, was expressed as the sum of the scattering rates due to normal and resistive scattering,

147 as follows:

148 $$\tau_c^{-1} = \tau_N^{-1} + \tau_R^{-1}.$$ (S6)

149 Here, the total resistive scattering rate, τ_R^{-1}, was expressed as the following:

150 $$\tau_R^{-1} = \tau_U^{-1} + \tau_B^{-1} + \tau_{Imp}^{-1} + \tau_{Intc}^{-1}.$$ (S7)

151 Finally, to determine the temperature dependence of the thermal conductivity of the samples before

152 and after intercalation quantitatively and qualitatively, a theoretical calculation (i.e., fitting) based on the

153 relaxation-time model using the following expression predicted by the Debye-Callaway[2] model in 1959

154 was used:

155 $$\kappa = \kappa_{debye} + \kappa_{callaway} = \frac{k_B{}^4 T^3}{2\pi^2 v\hbar^3} \int_0^{\frac{\theta_D}{T}} \frac{\tau_C x^4 e^x}{(e^x-1)^2} dx + \frac{k_B{}^4 T^3}{2\pi^2 v\hbar^3} \frac{\left(\int_0^{\frac{\theta_D}{T}} \frac{\tau_C x^4 e^x}{\tau_N (e^x-1)^2} dx\right)^2}{\int_0^{\frac{\theta_D}{T}} \frac{\tau_C x^4 e^x}{\tau_N \tau_R (e^x-1)^2} dx}$$ (S6.8)

156 where, k_B is the Boltzmann constant, $\hbar$ is the reduced Planck constant, v is the phonon group velocity, $x =$

157 $\frac{\hbar\omega}{k_B T}$, and θ_D is the Debye temperature that is estimated by $\theta_i = \frac{\hbar\omega}{k_B}$.

158

159 The Debye temperature of 900 K is reliably chosen as per reported in literature[3, 4] Note that the model fit is

160 not sensitive to changes in Debye temperature, so we decided to use the literature value instead of measuring

161 or making it a fitting parameter.

162   In the cross-plane direction, the thermal conductivity is predominantly due to phonon transport, as
163 electrons are less mobile between the weakly bonded layers. Given this established understanding[5] that
164 electronic contributions are negligible in this direction, our study only focused on investigating the phonon
165 contribution. This approach aligns with the observations by Dresselhaus et al. that the magnitude and
166 temperature dependence of the c-axis thermal conductivity of GIC preclude any electronic contribution in
167 this direction This enables ensuring that our analysis accurately reflects the dominant heat transport
168 mechanism in this direction.

Parameters	Units	Before intercalation	After intercalation
v	m/s	4050±87.2	2835±107
$d(\lambda_B)$	nm	450±6.3, 110±9.2, 30±2.1	710±20.9, 170±11.2, 45±3.9
$d(\lambda_{intc})$	nm	-	~3-5±0.23 (for 3 co-GICs)
B_N	s/K^3	1±0.61 × 10^{-24}	1±0.61 × 10^{-24}
B_U	s/K^3	5±0.35 × 10^{-22}	5±0.35 × 10^{-22}
A	s^3/m	230±18.4	230±18.4
α	-	3	3
θ_D	K	900	900

Table S6.1: Parameters used to fit TDTR data for all thicknesses and their uncertainties

S6.2: Goodness of fit for Debye-Callaway fittings

| (a) 30 nm graphite	(b) 45 nm GIC
R-squared: 0.980358	R-squared: 0.928690
RMSE: 0.003621	RMSE: 0.037064
Mean Absolute Error: 0.003133	Mean Absolute Error: 0.030024
(c) 110 nm graphite	(d) 170 nm GIC
R-squared: 0.963094	R-squared: 0.798802
RMSE: 0.025841	RMSE: 0.144153
Mean Absolute Error: 0.017759	Mean Absolute Error: 0.101374
(e) 450 nm graphite	(f) 710 nm GIC
R-squared: 0.785753	R-squared: 0.736909
RMSE: 0.051124	RMSE: 0.371925
Mean Absolute Error: 0.041479	Mean Absolute Error: 0.326828

Table S6.2: Goodness of fit for all the fitting curves

The low RMSE values in our fits suggest a close fit between the model and actual observed values, with small mean error magnitudes.
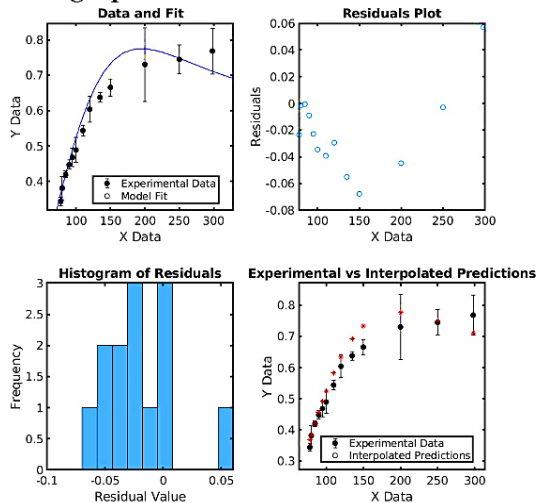
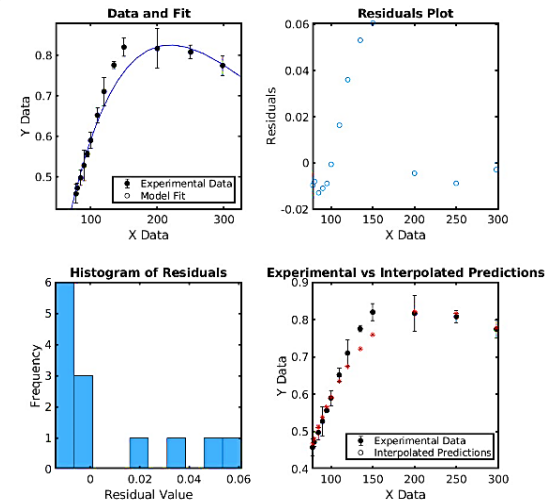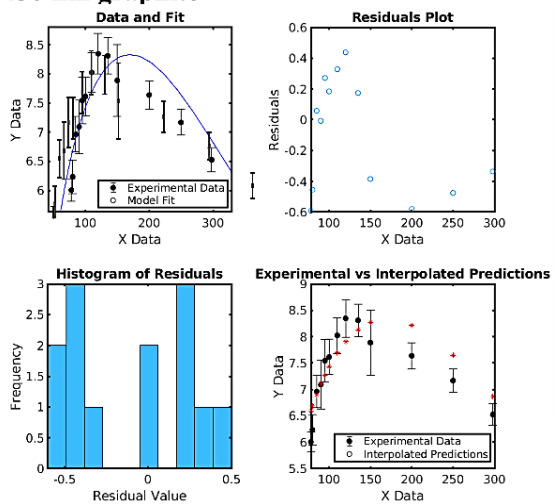**(a) 30 nm graphite**

(b) 45 nm GIC
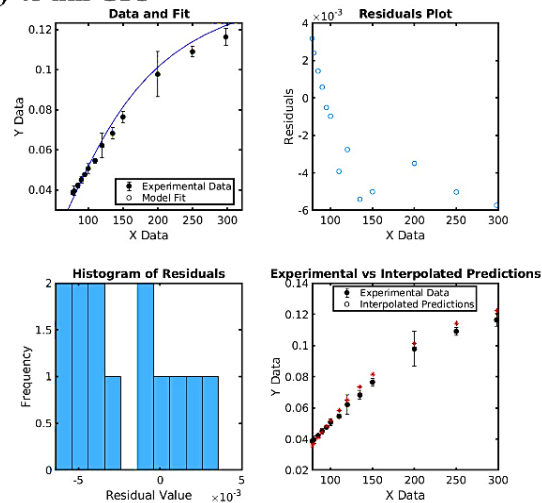
(c) 110 nm Graphite
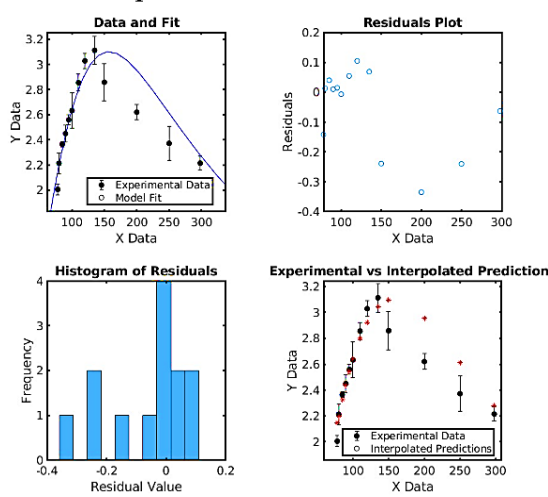
(d) 170 nm GIC
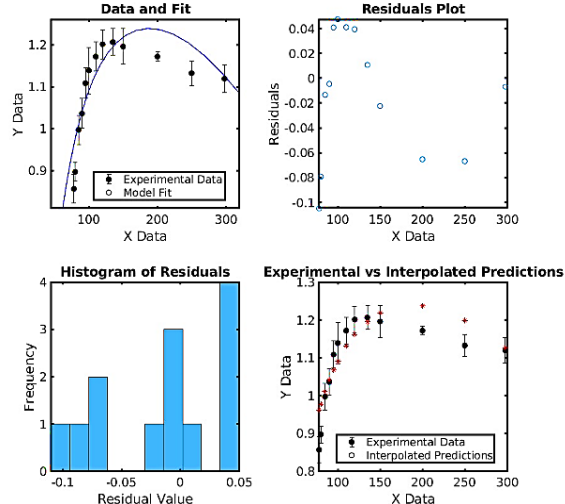
(e) 450 nm graphite

(f) 710 nm GIC

Figure S6.1: Uncertainty analysis of the theoretical model fit to each sample data and relevant statistical plots for pristine and intercalated counterparts.
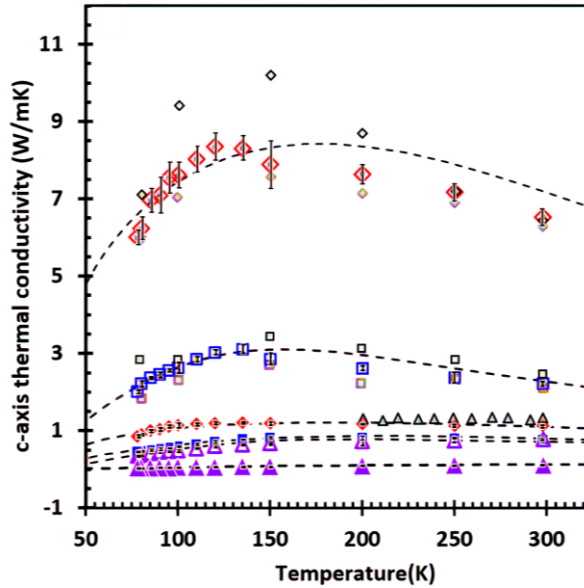
216

217

Figure S6.2: Measured data fitted to the Debye–Callaway model to investigate the temperature dependence of κ_z of graphite and the GIC counterparts in the linear-scale. The log scale data is presented in Figure 4 in main text with corresponding legend.

218

S6.3: Reduction in effective ε (LJ potential parameter) upon intercalation softens phonon c-axis group velocity

221

The *12-6* Lennard-Jones *(LJ)* potential is given by:

$$V_{LJ}(r) = 4\varepsilon \left[\left(\frac{\sigma}{r} \right)^{12} - \left(\frac{\sigma}{r} \right)^{6} \right] \tag{S8}$$

where ε is the depth of the potential well, σ is the finite distance at which the interparticle potential is zero, and r is the distance between the particles. In the context of the interaction between C and MnCl$_2$, a Waldman-Hagler mixing law[6] is used to calculate the combined epsilon (ε) for the interacting species based on the individual ε and σ values of C, Cl, and Mn[7]. The formula for the mixing law is:

$$\epsilon_{ij} = \frac{2\sqrt{\epsilon_i \epsilon_j} \sigma_i^3 \sigma_j^3}{\sigma_i^6 + \sigma_j^6} \tag{S9}$$

229   • ϵ_{ij} is the effective depth of the potential well for the interaction between i and j.

230   • σ_{ij} is the effective distance at which the potential energy is zero for interaction between i and j.

231   • ϵ_i, ϵ_j are the depth of the potential wells for i and j, respectively.

232   • σ_i, σ_j are the distances at which the potential energy is zero for i and j, respectively.

233 Applying this to the given data (ε and σ values for C, Cl and Mn[1] ;ε_C = 7.3×10^{-22} J/atom, σ_C = 3.40 Å, ε_{Cl} =

234 1.8×10^{-21} J/atom, σ_{Cl} = 4.40 Å, ε_{Mn} = 9.1×10^{-23} J/atom, σ_{Mn} = 2.50 Å) and considering the effectiveness of

235 the LJ potential diminishes with distance and since MnCl$_2$ is intercalated between graphene layers, not all

236 atoms of MnCl$_2$ are in close proximity to C atoms, leading to a varying degree of interaction strength making

237 only the nearest pairwise interaction significant. The effective averaged out ε value for the C-MnCl$_2$

238 interaction can then be given by $\epsilon_{C-MnCl2} = \frac{\epsilon_{C-Cl} \times 2 + \epsilon_{C-Mn}}{3}$ is about 5.8 × 10^{-22} J/atom which is a 21% drop

239 when compared to the ε value for C-C interaction in graphene, ϵ_{C-C} which is 7.3 × 10^{-22} J/atom. This

240 reduction signifies the softening of the C-C interaction in the presence of MnCl$_2$ intercalation within

241 graphene layers implying a reduction in the strength of bonding forces and thus phonon velocity. Note that

242 since the number density of crystalline MnCl$_2$ layer is smaller than that of graphene, the actual contrast is

243 expected to be higher.

244

References

246 (1) Maznev, A.; Wright, O. Demystifying umklapp vs normal scattering in lattice thermal conductivity. *American*
247 *journal of physics* **2014**, *82* (11), 1062-1066.
248 (2) Callaway, J. Model for lattice thermal conductivity at low temperatures. *Physical Review* **1959**, *113* (4), 1046.
249 (3) Krumhansl, J.; Brooks, H. The lattice vibration specific heat of graphite. *The Journal of Chemical Physics* **1953**, *21*
250 (10), 1663-1669.
251 (4) Bowman, J.; Krumhansl, J. The low-temperature specific heat of graphite. *Journal of Physics and Chemistry of*
252 *Solids* **1958**, *6* (4), 367-379.
253 (5) Issi, J.-P.; Heremans, J.; Dresselhaus, M. Electronic and lattice contributions to the thermal conductivity of graphite
254 intercalation compounds. *Physical Review B* **1983**, *27* (2), 1333.
255 (6) Waldman, M.; Hagler, A. T. New combining rules for rare gas van der Waals parameters. *Journal of computational*
256 *chemistry* **1993**, *14* (9), 1077-1084.
257 (7) *Lennard-Jones Force Fields and potential energy. forcefields.* 2021.
258 https://simonensemble.github.io/PorousMaterials.jl/dev/force_field/ (accessed 231015).
259